Parallel FDTD Modeling of Nonlocality in Plasmonics

Joshua Baxter [ID], Antonio Calà Lesina [ID], and Lora Ramunno

Abstract—As nanofabrication techniques become more precise, with ever smaller feature sizes, the ability to model nonlocal effects in plasmonics becomes increasingly important. Although nonlocal models based on hydrodynamics have been implemented using various computational electromagnetics techniques, the finite-difference time-domain (FDTD) version has remained elusive. Here, we present a comprehensive FDTD implementation of nonlocal hydrodynamics, including parallel computing. As a subnanometer step size is required to resolve nonlocal effects, a parallel implementation makes the computational cost of nonlocal FDTD more affordable. We first validate our algorithms for small spherical metallic particles, and find that nonlocality smears out staircasing artifacts at metal surfaces, increasing the accuracy over local models. We find this also for a larger nanostructure with sharp extrusions. The large size of this simulation, where nonlocal effects are clearly present, highlights the importance and impact of a parallel implementation in FDTD.

Index Terms—Finite-difference time-domain (FDTD), generalized nonlocal optical response (GNOR), hydrodynamic plasma model, nonlocality, parallel computing, plasmonics.

I. INTRODUCTION

FABRICATING objects with nanoscale precision is possible due to significant progress in nanofabrication techniques over the last few decades [1]. As a result, plasmonic nanostructures and metamaterials [2] are having tremendous impact on many fields including biosensing [3], quantum cryptography [4], nonlinear optics [5], photovoltaics [6], light emitting devices [7], and precision medicine [8].

Numerical modeling in plasmonics is typically based on optical models for bulk permittivity. These models—such as the Drude model for free-electron response, and the Lorentz and critical points models for bound electron response [9], [10]—are based on the local response approximation (LRA), which assumes that the induced polarization or current at a given location depends only on the electromagnetic field at

that same location. While appropriate for many applications, the Drude model is insufficient for modeling plasmonic structures smaller than 10 nm [11]–[14], as well as those containing sharp features or nanoscale gaps [15], [16]. The charge density near the surface of plasmonic objects is spread over a finite thickness on the order of a few angstroms [16], [17], and thus for small features, cannot be treated as localized at the surface, as is implicit in LRA models.

The hydrodynamic plasma model treats the conduction band electrons as a free electron gas [5], [12], [16]–[18], accounting for free-electron fluctuations via a pressure term. Unlike the Drude model, it does not make an LRA and thus nonlocality is incorporated. It has been found to correctly predict the expected spread of charge density near plasmonic surfaces as well as predict the blueshift in plasmon resonance with decreasing particle size [13], [17], [19]. More recently, the effects of electron diffusion were incorporated within a generalized nonlocal optical response (GNOR) model, correctly predicting a broadened line shape that was observed experimentally [20].

Nonlocal hydrodynamic models have been implemented using several computational electromagnetic methods including the finite element method [21], the discontinuous Galerkin time-domain (DGTD) method [22], and the boundary element method [23]. Due to their inhomogeneous mesh, finite element methods, including DGTD, offer computationally efficient calculations for systems containing sharp features, or complex geometry, especially when compared to finite difference methods. This has been demonstrated for dielectric resonator simulations [24]. However, the complexity of implementation of such methods, and a dearth of reliable open source code, may present a hurdle for researchers in the field.

A finite-difference time-domain (FDTD) implementation of nonlocal plasmonic models would be advantageous due to the widespread use of FDTD in the photonics community, its relative ease of implementation, the availability of reliable open source codes [25], its broadband capabilities, its ability to produce time-domain movies, and its near-linear scalability when run on many processors [26]. Few attempts have been made [27]–[29], however none of them consider high-performance computing and parallel implementations, nor include electron diffusion. In addition, one uses an erroneous approximation, and another deals with terahertz plasmonics. A correct and comprehensive FDTD implementation for plasmonics within and near the visible regime has remained unreported.

In this article, we present a parallel FDTD implementation of nonlocal hydrodynamics, including a GNOR implementation. A parallel implementation in FDTD is especially

important for simulating nonlocality, as the grid cell size needs to be smaller than the Fermi wavelength $\lambda_F \sim 0.5$ nm to capture the spread of electron density [30]. This can require a large amount of memory and can present a prohibitive computational load. High-performance computing represents a viable solution. The FDTD rectangular-meshing scheme, where a field update at one location requires fields only in adjacent Yee-cells [31], lends itself well to parallel computing; indeed, message passing interface (MPI)-based FDTD solvers are well reported for LRA models [26]. Furthermore, high-performance computing is becoming more accessible with cloud computing, computing consortiums, increased high-performance computing investments, and new, higher-level parallel programming languages such as Chapel [32].

The structure of this article is as follows. We review nonlocal hydrodynamics in Section II, including the most common version without electron diffusion, as well as GNOR, which does include electron diffusion. In Section III, we derive from the nonlocal models FDTD update equations for the polarization field via the auxiliary differential equation (ADE) method. In Section IV, we discuss the implementation of the nonlocal FDTD update equations for parallel computing within an MPI framework. In Section V, we test our implementations by simulating the optical response of small metallic nanospheres and comparing our results to analytic solutions and experimental results. We find an unexpected benefit of nonlocal versus LRA modeling: a marked decrease in staircasing artifacts at the metal boundary. Due to the rectangular discretization inherent in most FDTD approaches, fields can build up in an unphysical manner at plasmonic surfaces, and this can be particularly problematic in applications that rely on plasmonic near-field enhancement [33]. The incorporation of nonlocality significantly decreases this unphysical field build-up. In Section VI, we simulate the response from a spherical nanoparticle-containing sharp extrusions as a demonstration of a large-scale simulation that requires both parallel computing and nonlocal modeling. We find that despite the nanoparticle being larger, the sharp extrusions exhibit plasmonic features not accessible to the LRA. Finally, in Section VII, we give concluding remarks.

II. HYDRODYNAMIC MODELS FOR NONLOCALITY

The most general response of a linear optical material to incident radiation is described by

$$\mathbf{D}(\mathbf{r}, \omega) = \varepsilon_0 \int \varepsilon(\mathbf{r}, \mathbf{r}', \omega) \mathbf{E}(\mathbf{r}', \omega) d\mathbf{r}' \qquad (1)$$

where the dielectric function of the material, $\varepsilon(\mathbf{r}, \mathbf{r}', \omega)$, is nonlocal when the displacement field $\mathbf{D}$ at one location depends on the electric field $\mathbf{E}$ at other locations. In many applications, it is appropriate to use a LRA, wherein $\varepsilon(\mathbf{r}, \mathbf{r}', \omega) = \delta(\mathbf{r} - \mathbf{r}')\varepsilon(\omega)$. In plasmonic modeling, the interaction of the electric field and the free electron plasma is typically described by the Drude model, which employs the LRA, where the dielectric function reduces to [9]

$$\varepsilon(\omega) = 1 - \frac{\omega_p^2}{\omega^2 + i\gamma\omega} \qquad (2)$$

where ω_p is the plasma frequency, γ is a collisional damping rate, and i is the imaginary unit.

The hydrodynamic plasma model [17] goes beyond the LRA, more accurately describing spatial–temporal free electron dynamics via

$$\frac{\partial \mathbf{v}}{\partial t} + (\mathbf{v} \cdot \nabla)\mathbf{v} = -\frac{e}{m}(\mathbf{E} + \mathbf{v} \times \mathbf{B}) - \gamma\mathbf{v} - \frac{1}{m}\nabla\frac{\delta G[n]}{\delta n} \qquad (3)$$

where $\mathbf{v}$ is the velocity field of the free electron plasma, $\mathbf{E}$ and $\mathbf{B}$ are the electric and magnetic fields, and n is the free electron density. The energy functional $G[n]$ considers the internal kinetic energy of the electron gas and is usually taken to be the Thomas–Fermi functional, giving

$$\frac{\delta G[n]}{\delta n} = \frac{h^2}{2m}\left(\frac{3}{8\pi}n\right)^{\frac{2}{3}} \qquad (4)$$

where h is Planck's constant. As we are only considering the linear nonlocal response in this article, we neglect the nonlinear terms (magnetic-Lorentz and convection) in (3) giving

$$\frac{\partial \mathbf{v}}{\partial t} + \gamma\mathbf{v} = -\frac{e}{m}\mathbf{E} - \frac{\beta^2}{n}\nabla n \qquad (5)$$

where $\beta^2 = (1/3\ v_F^2)$ and v_F is the Fermi velocity. The free electron density fluctuations are accounted for in the last term of (5). This is often referred to as the pressure term, and is responsible for the known blue shift in the surface plasmon resonance with decreasing particle size [13], [17]. Along with this formula for the velocity field, we require the continuity equation given by

$$\frac{\partial n}{\partial t} = -\nabla \cdot (n\mathbf{v}). \qquad (6)$$

From here, we consider two approaches. The first is the most widely used and assumes a current density given by $\mathbf{J} = -en\mathbf{v}$. As we use a polarization field formulation in this article, we set $\mathbf{J} = (\partial \mathbf{P}_{NL}/\partial t)$, where we have defined $\mathbf{P}_{NL}$ to be the (nonlocal) free electron polarization field. The velocity field is thus $\mathbf{v} = -(1/ne)\ (\partial \mathbf{P}_{NL}/\partial t)$, and (6) becomes

$$n = n_0 + \frac{1}{e}\nabla \cdot \mathbf{P}_{NL} \qquad (7)$$

where n_0 is the equilibrium free electron density. From (5), we then obtain

$$\frac{\partial^2 \mathbf{P}_{NL}}{\partial t^2} + \gamma\frac{\partial \mathbf{P}_{NL}}{\partial t} = \varepsilon_0\omega_p^2\mathbf{E} + \beta^2\nabla(\nabla \cdot \mathbf{P}_{NL}) \qquad (8)$$

where $\omega_p = \sqrt{(e^2 n_0/m\varepsilon_0)}$. We call (8) the "nonlocal Drude model" because it consists of the classical LRA Drude model plus one additional term that gives rise to nonlocality (i.e., the term proportional to β^2).

The model represented by (8) differs from those used in the three previous nonlocal FDTD works. In Ref. [27], the gradient-divergence term was simplified to a Laplacian, and this resulted in spurious, nonphysical resonances [18]. In Ref. [23], a current density formulation is used. A benefit to using a polarization field formulation is that it gives ready access to the free electron density via Gauss's Law, as we demonstrate in Section V. In Ref. [29], the thermal kinetic

energy is used instead of the Fermi energy in the pressure term. Because we are interested in plasmonics within and near the visible regime with noble metals, we need to use the Fermi energy since $E_F \approx 215 \, K_B T$ at room temperature. It is worth noting that Ref. [34] introduces an explicit scheme to solve (3) via FDTD for nonlinear plasmonics without the Thomas–Fermi functional, which is the only nonlocal term that is relevant for linear simulations.

The second approach we consider includes electron diffusion, which was also found to play an important role in the optical response of small metallic particles [20]. This has been described by the GNOR model, where diffusion is considered by modifying the expression for the velocity field via $\mathbf{v} = (-1/en)((\partial \mathbf{P}_G/\partial t) + \mathcal{D}\nabla(\nabla \cdot \mathbf{P}_G))$, where $\mathcal{D}$ is the diffusion coefficient and where we have denoted the GNOR free electron polarization field by $\mathbf{P}_G$.

Using in (5) and (6) the GNOR definition for the velocity field, we obtain the following time-domain nonlocal-diffusive hydrodynamics model for the polarization field, which we hereafter refer to as the "GNOR" model:

$$\frac{\partial^2 \mathbf{P}_G}{\partial t^2} + \gamma \frac{\partial \mathbf{P}_G}{\partial t} = \varepsilon_0 \omega_p^2 \mathbf{E} + \eta \nabla(\nabla \cdot \mathbf{P}_G) + \mathcal{D}\frac{\partial}{\partial t}\nabla(\nabla \cdot \mathbf{P}_G) \quad (9)$$

where $\eta = \beta^2 + \mathcal{D}\gamma$. GNOR correctly predicts both the blueshift in the plasmon resonance frequency as well as the broadening of the absorption peak with decreasing particle size. The broadening is the result of the diffusion coefficient, but it is worth noting that this effect can be introduced through other models. For example, one can increase the Drude damping coefficient phenomenologically as a function of nanoparticle size to account for electron scattering from the particle surface [35]. One may also introduce a stress tensor term into the hydrodynamic model [36]. In this article, we will consider only the nonlocal Drude and GNOR models (both of which are thoroughly reviewed in Ref. [17]).

It is from (8) and (9) that we derive in Section III, our FDTD update equations for implementing the two different models of the free electron response of plasmonic material, one accounting for nonlocality only (8), and the other nonlocality with diffusion (9).

To properly model the optical response of many plasmonic materials, one must also include the contribution of interband transitions through bound electrons. We employ the LRA-based N-critical points model that assumes a susceptibility of the form

$$\chi_{CP}(\omega) = (\varepsilon_\infty - 1)$$
$$+ \sum_{p=1}^{N} A_p \Omega_p \left(\frac{e^{i\phi_p}}{\Omega_p - \omega - i\Gamma_p} + \frac{e^{-i\phi_p}}{\Omega_p + \omega + i\Gamma_p} \right) \quad (10)$$

where ε_∞ is the infinite frequency permittivity, and A_p, Ω_p, Γ_p, and ϕ_p are fitting parameters. This model can be readily transformed to the time-domain for FDTD implementation, as described in detail in Ref. [37].

III. UPDATE EQUATIONS FOR NONLOCAL FDTD

We derive in this section the FDTD update equations for the time-domain nonlocal Drude and GNOR models

TABLE I
YEE CELL POSITIONS OF THE ELECTRIC, MAGNETIC, AND POLARIZATION FIELDS

	Electric	Magnetic	Polarization
E_x, H_x, P_x	i+1/2, j, k	i, j+1/2, k+1/2	i+1/2, j, k
E_y, H_y, P_y	i, j+1/2, k	i+1/2, j, k+1/2	i, j+1/2, k
E_z, H_z, P_z	i, j, k+1/2	i+1/2, j+1/2, k	i, j, k+1/2

[(8) and (9), respectively], using the ADE method. We also present the update equations for the N-critical points model (10) to account for interband transitions which is derived elsewhere [37].

We discretize our domain via the Yee cell [31] where the electric fields are collocated with the polarization fields in time and space; the Yee cell positions of the electric, magnetic, and polarization fields used in this article are listed in Table I. We denote the free-electron polarization field by $\mathbf{P}_f$ (which signifies either $\mathbf{P}_{NL}$ or $\mathbf{P}_G$), and the bound electron polarization field by $\mathbf{P}_{CP}$.

The FDTD update algorithm at time $= n\Delta t$, where Δt is the time step size, consists of updating (in order) the:

1) magnetic field $\mathbf{H}^{n+1/2} = f_1(\mathbf{H}^{n-1/2}, \mathbf{E}^n)$,
2) electric field $\mathbf{E}^{n+1} = f_2(\mathbf{E}^n, \mathbf{P}_f^n, \mathbf{P}_{CP}^n, \mathbf{H}^{n+1/2})$,
3) bound charge polarization $\mathbf{P}_{CP}^{n+1} = f_3(\mathbf{E}^{n+1}, \mathbf{P}_{CP}^n)$,
4) free charge polarization $\mathbf{P}_f^{n+1} = f_4(\mathbf{E}^{n+1}, \mathbf{P}_f^n)$,

via update equations f_1, f_2, f_3, and f_4, whose form and required inputs depend on the model from which they are derived. The equation f_1 is the magnetic field update derived through discretization of the Maxwell–Faraday equation [38]; we do not derive this here because in plasmonic simulations it is typically unchanged from the vacuum equation. In what follows, we present the electric field update equation f_2 (derived from the Maxwell–Ampère law), the bound charge polarization update equation f_3 [derived from (10)], and the free charge polarization update f_4 (derived from (8) for the nonlocal Drude model, and (9) for the GNOR model). Though we present f_4 for two nonlocal models, one must choose which to use—they cannot be used simultaneously.

We start by deriving f_4 from the nonlocal Drude model. Using central differencing, we discretize (8) centered at time $n\Delta t$, to obtain

$$\frac{\mathbf{P}_{NL}^{n+1} - 2\mathbf{P}_{NL}^n + \mathbf{P}_{NL}^{n-1}}{\Delta t^2} + \gamma \frac{\mathbf{P}_{NL}^{n+1} - \mathbf{P}_{NL}^{n-1}}{2\Delta t} = \varepsilon_0 \omega_p^2 \mathbf{E}^n + \beta^2 \nabla(\nabla \cdot \mathbf{P}_{NL}^n). \quad (11)$$

Furthermore, using weighted central averaging as discussed in Ref. [33], we set $\mathbf{E}^n = (\mathbf{E}^{n-1} + 2\mathbf{E}^n + \mathbf{E}^{n+1})/4$ to obtain

$$\mathbf{P}_{NL}^{n+1} = D_1 \mathbf{P}_{NL}^n + D_2 \mathbf{P}_{NL}^{n-1} + D_3 (\mathbf{E}^{n-1} + 2\mathbf{E}^n + \mathbf{E}^{n+1}) + D_{NL}\nabla(\nabla \cdot \mathbf{P}_{NL}^n) \quad (12)$$

where

$$D_1 = \frac{2}{D_d \Delta t^2} \quad (13)$$

$$D_2 = \frac{1}{D_d}\left(\frac{\gamma}{2\Delta t} - \frac{1}{\Delta t^2} \right) \quad (14)$$

$$D_3 = \frac{\varepsilon_0 \omega_p^2}{4 D_d} \tag{15}$$

$$D_{NL} = \frac{\beta^2}{D_d} \tag{16}$$

$$D_d = \left(\frac{\gamma}{2 \Delta t} + \frac{1}{\Delta t^2} \right). \tag{17}$$

As the x, y, and z components of $\nabla(\nabla \cdot \mathbf{P}_{NL}^n)$ must be collocated with the x, y, and z components of $\mathbf{P}_{NL}$, we have

$$
\begin{aligned}
&\nabla(\nabla \cdot \mathbf{P}_{NL}^n)\big|_x^{i+1/2,j,k} \\
&= \frac{\partial}{\partial x}\left(\frac{\partial P_x}{\partial x} + \frac{\partial P_y}{\partial y} + \frac{\partial P_z}{\partial z} \right)\bigg|_x^{i+1/2,j,k} \\
&\approx \frac{P_x^{i+3/2,j,k} - 2 P_x^{i+1/2,j,k} + P_x^{i-1/2,j,k}}{\Delta x^2} \\
&+ \frac{P_y^{i+1,j+1/2,k} - P_y^{i+1,j-1/2,k} - P_y^{i,j+1/2,k} + P_y^{i,j-1/2,k}}{\Delta x \Delta y} \\
&+ \frac{P_z^{i+1,j,k+1/2} - P_z^{i+1,j,k-1/2} - P_z^{i,j,k+1/2} + P_z^{i,j,k-1/2}}{\Delta x \Delta z}
\end{aligned}
\tag{18a}
$$

$$
\begin{aligned}
&\nabla(\nabla \cdot \mathbf{P}_{NL}^n)\big|_y^{i,j+1/2,k} \\
&= \frac{\partial}{\partial y}\left(\frac{\partial P_x}{\partial x} + \frac{\partial P_y}{\partial y} + \frac{\partial P_z}{\partial z} \right)\bigg|_y^{i,j+1/2,k} \\
&\approx \frac{P_y^{i,j+3/2,k} - 2 P_y^{i,j+1/2,k} + P_y^{i,j-1/2,k}}{\Delta y^2} \\
&+ \frac{P_x^{i+1/2,j+1,k} - P_x^{i-1/2,j+1,k} - P_x^{i+1/2,j,k} + P_x^{i-1/2,j,k}}{\Delta x \Delta y} \\
&+ \frac{P_z^{i,j+1,k+1/2} - P_z^{i,j+1,k-1/2} - P_z^{i,j,k+1/2} + P_z^{i,j,k-1/2}}{\Delta y \Delta z}
\end{aligned}
\tag{18b}
$$

$$
\begin{aligned}
&\nabla(\nabla \cdot \mathbf{P}_{NL}^n)\big|_z^{i,j,k+1/2} \\
&= \frac{\partial}{\partial z}\left(\frac{\partial P_x}{\partial x} + \frac{\partial P_y}{\partial y} + \frac{\partial P_z}{\partial z} \right)\bigg|_z^{i,j,k+1/2} \\
&\approx \frac{P_z^{i,j,k+3/2} - 2 P_z^{i,j,k+1/2} + P_z^{i,j,k-1/2}}{\Delta z^2} \\
&+ \frac{P_x^{i+1/2,j,k+1} - P_x^{i-1/2,j,k+1} - P_x^{i+1/2,j,k} + P_x^{i-1/2,j,k}}{\Delta x \Delta z} \\
&+ \frac{P_y^{i,j+1/2,k+1} - P_y^{i,j-1/2,k+1} - P_y^{i,j+1/2,k} + P_y^{i,j-1/2,k}}{\Delta y \Delta z}
\end{aligned}
\tag{18c}
$$

where, for brevity, the components of $\mathbf{P}_{NL}$ are written as P_a for $a = x, y, z$.

For the GNOR model, the f_4 update equation includes (12)–(18) (with β^2 replaced by η) along with a suitable discretization for the last term of (9), the only term that does not appear in the nonlocal Drude model. As this term cannot be achieved via central differencing, we use an alternate second order backward finite difference scheme given in Table 3 of Ref. [39]

$$
\frac{\partial}{\partial t} \nabla(\nabla \cdot \mathbf{P}_G^n) \approx \frac{3\nabla(\nabla \cdot \mathbf{P}_G^n) - 4\nabla(\nabla \cdot \mathbf{P}_G^{n-1}) + \nabla(\nabla \cdot \mathbf{P}_G^{n-2})}{2\Delta t}.
\tag{19}
$$

The GNOR f_4 update then becomes

$$
\begin{aligned}
\mathbf{P}_G^{n+1} &= D_1 \mathbf{P}_G^n + D_2 \mathbf{P}_G^{n-1} + D_3\left(\mathbf{E}^{n-1} + 2\mathbf{E}^n + \mathbf{E}^{n+1} \right) \\
&+ D_{G1} \nabla(\nabla \cdot \mathbf{P}_G^n) \\
&+ D_{G2}\left(3\nabla(\nabla \cdot \mathbf{P}_G^n) - 4\nabla(\nabla \cdot \mathbf{P}_G^{n-1}) + \nabla(\nabla \cdot \mathbf{P}_G^{n-2}) \right)
\end{aligned}
\tag{20}
$$

where

$$D_{G1} = \frac{\eta}{D_d} \tag{21}$$

$$D_{G2} = \frac{\mathcal{D}}{2 \Delta t D_d}. \tag{22}$$

The f_3 update equation for the bound charge polarization field is derived from the critical points model (10) in Ref. [37]. We state it here

$$\mathbf{P}_{CP,p}^{n+1} = C_{1p} \mathbf{P}_{CP,p}^n + C_{2p} \mathbf{P}_{CP,p}^{n-1} + C_{3p} \mathbf{E}^{n+1} + C_{4p} \mathbf{E}^n + C_{5p} \mathbf{E}^{n-1} \tag{23}$$

where

$$C_{1p} = \frac{1}{C_p}\left(\frac{2}{\Delta t^2} - \frac{\Omega_p^2 + \Gamma_p^2}{2} \right) \tag{24}$$

$$C_{2p} = \frac{1}{C_p}\left(\frac{\Gamma_p}{\Delta t} - \frac{1}{\Delta t^2} - \frac{\Omega_p^2 + \Gamma_p^2}{4} \right) \tag{25}$$

$$C_{3p} = \frac{C_{4p}}{2} - \frac{\varepsilon_0 A_p \Omega_p \sin \phi_p}{2 \Delta t C_p} \tag{26}$$

$$C_{4p} = \frac{\varepsilon_0 A_p \Omega_p \left(\Omega_p \cos \phi_p - \Gamma_p \sin \phi_p \right)}{C_p} \tag{27}$$

$$C_{5p} = \frac{C_{4p}}{2} + \frac{\varepsilon_0 A_p \Omega_p \sin \phi_p}{2 \Delta t C_p} \tag{28}$$

$$C_p = \frac{\Gamma_p}{\Delta t} + \frac{1}{\Delta t^2} + \frac{\Omega_p^2 + \Gamma_p^2}{4} \tag{29}$$

where p denotes the pth critical point.

Next we turn to the f_2 update equation for $\mathbf{E}^{n+1}$. Ampère's law is discretized in time to give

$$
\begin{aligned}
\varepsilon_0 \varepsilon_\infty \frac{\mathbf{E}^{n+1} - \mathbf{E}^n}{\Delta t} &+ \frac{\mathbf{P}_f^{n+1} - \mathbf{P}_f^n}{\Delta t} \\
&+ \sum_{p=1}^{N} \frac{(\mathbf{P}_{CP,p}^{n+1} - \mathbf{P}_{CP,p}^n)}{\Delta t} = \nabla \times \mathbf{H}^{n+1/2}.
\end{aligned}
\tag{30}
$$

For the nonlocal Drude model we set $\mathbf{P}_f = \mathbf{P}_{NL}$, and plug (12) into (30) to obtain

$$
\begin{aligned}
\mathbf{E}^{n+1} &\left(\varepsilon_0 \varepsilon_\infty + D_3 + \sum_{p=1}^{N} C_{3p} \right) \\
&= \Delta t\left(\nabla \times \mathbf{H}^{n+1/2} \right) \\
&+ \left(\varepsilon_0 \varepsilon_\infty - 2D_3 + \sum_{p=1}^{N} C_{4p} \right) \mathbf{E}^n \\
&- \left(D_3 + \sum_{p=1}^{N} C_{5p} \right) \mathbf{E}^{n-1} - (D_1 - 1) \mathbf{P}_{NL}^n
\end{aligned}
$$

$$-\sum_{p=1}^{N}(C_{1p}-1)\mathbf{P}_{CP,p}^{n} - D_2\mathbf{P}_{NL}^{n-1}$$

$$-\sum_{p=1}^{N}C_{2p}\mathbf{P}_{CP,p}^{n-1} - D_{NL}\nabla(\nabla\cdot\mathbf{P}_{NL}^{n}). \tag{31}$$

For the GNOR model we set $\mathbf{P}_f = \mathbf{P}_G$, and plug (20) into (30) to obtain

$$\mathbf{E}^{n+1}\left(\varepsilon_0\varepsilon_\infty + D_3 + \sum_{p=1}^{N}C_{3p}\right)$$

$$= \Delta t(\nabla\times\mathbf{H}^{n+1/2}) + \left(\varepsilon_0\varepsilon_\infty - 2D_3 + \sum_{p=1}^{N}C_{4p}\right)\mathbf{E}^n$$

$$-\left(D_3 + \sum_{p=1}^{N}C_{5p}\right)\mathbf{E}^{n-1}$$

$$-(D_1-1)\mathbf{P}_G^n - \sum_{p=1}^{N}(C_{1p}-1)\mathbf{P}_{CP,p}^n - D_2\mathbf{P}_G^{n-1}$$

$$-\sum_{p=1}^{N}C_{2p}\mathbf{P}_{CP,p}^{n-1} - D_{G1}\nabla(\nabla\cdot\mathbf{P}_G^n)$$

$$-D_{G2}\left(3\nabla(\nabla\cdot\mathbf{P}_G^n) - 4\nabla(\nabla\cdot\mathbf{P}_G^{n-1}) + \nabla(\nabla\cdot\mathbf{P}_G^{n-2})\right). \tag{32}$$

For the GNOR update, to avoid recalculation of $\nabla(\nabla\cdot\mathbf{P}_G^{n-1})$, and $\nabla(\nabla\cdot\mathbf{P}_G^{n-2})$, we store them in arrays; therefore GNOR requires additional memory.

The update equations derived above must be implemented in all cells in which the plasmonic material exists. However, care needs to be taken if the nonlocal material extends to the boundary of the simulation domain. Terminating a non-local material with a perfectly matched layer (PML) may result in instability and convergence issues. Within a total field/scattered field (TF/SF) framework—which is applicable to many plasmonic nanostructure scattering problems—this can be overcome by using the nonlocal model only in the total field region. If TF/SF cannot be used, such as for geometries that include a plasmonic substrate, one may use the LRA Drude model in the PML region, and the nonlocal models everywhere else.

Finally, we would like to highlight that since the polarization fields are nonlocal, an additional boundary condition is required at the interface between the plasmonic and external media. In the FDTD implementation, material boundary conditions are implicitly imposed by not applying the plasmonic material update equations outside of the plasmonic material. Thus, the free electron density necessarily vanishes just outside the material boundaries. This implies that $\mathbf{P}_f \cdot \mathbf{n} = 0$ at the material boundary, where $\mathbf{n}$ is the unit vector normal to the boundary; however, the tangential component of $\mathbf{P}_f$ does not vanish at the material boundary [18]. We have confirmed numerically that our code implementation indeed implicitly imposes this additional boundary condition.

TABLE II
SUBDOMAIN UPDATE SCHEME FOR DIFFERENT FIELD COMPONENTS

Component	x dimension	y dimension	z dimension
E_x and P_x	$0 \to N_x - 1$	$1 \to N_y$	$1 \to N_z$
E_y and P_y	$1 \to N_x$	$0 \to N_y - 1$	$1 \to N_z$
E_z and P_z	$1 \to N_x$	$1 \to N_y$	$0 \to N_z - 1$
H_x	$1 \to N_x$	$0 \to N_y - 1$	$0 \to N_z - 1$
H_y	$0 \to N_x - 1$	$1 \to N_y$	$0 \to N_z - 1$
H_z	$0 \to N_x - 1$	$0 \to N_y - 1$	$1 \to N_z$

IV. PARALLEL IMPLEMENTATION OF NONLOCAL FDTD

In this section, we describe a parallel FDTD scheme using the MPI framework. Nonlocal simulations require a lot of memory since the step-size Δx needs to be smaller than the Fermi wavelength. In turn, significant computation time is required because the Courant–Friedrichs–Lewy condition restricts the time-step Δt according to Δx. Parallel computing thus becomes essential.

The simulation domain is decomposed into $n_x \times n_y \times n_z$ MPI processes where n_d is the number of MPI processes in the d direction, with $d = x, y, z$. Each MPI process is identified by a vector (m_x, m_y, m_z) which gives its relative spatial position within the simulation domain, where $0 \le m_d < n_d$.

Each process performs field updates within its own subdomain (i.e., its section of the simulation domain) defined according to a local grid with $(N_x + 1) \times (N_y + 1) \times (N_z + 1)$ points. The vector (i, j, k) identifies an individual grid cell within the local grid, where i ranges from 0 to N_x, j from 0 to N_y, and k from 0 to N_z, inclusively. The electric and magnetic field components at (i, j, k) correspond to different locations in physical space within the grid cell, according to the Yee cell shown in Table I. For example, $E_x(i, j, k)$ refers to $E_x(i\Delta x + \Delta x/2, j\Delta y, k\Delta z)$, whereas $E_y(i, j, k)$ refers to $E_y(i\Delta x, j\Delta y + \Delta y/2, k\Delta z)$.

The use of domain decomposition requires that data from the boundaries of subdomains be transferred to other subdomains at each time step. For subsequent updates to be executed efficiently, an overlap of information is required between adjacent subdomains. For example, the cells (N_x, j, k) in subdomain (m_x, m_y, m_z) represents the same physical locations as the cells $(0, j, k)$ in subdomain $(m_x + 1, m_y, m_z)$. The update scheme we describe below guarantees that the update equations for a given field component at a given physical location are only applied once.

The components of the magnetic and electric fields in a subdomain are updated via f_1 and f_2, respectively, however, each is updated for different ranges of indices (i, j, k) as summarized in Table II. The notation $0 \to N_d$ means we update from index 0 to index N_d, inclusively. Bound and free charge polarization fields are updated via f_3 and f_4, respectively, for the same ranges of indices as for the electric field, as listed in Table II. To understand this visually, the field update regions for the x and y components of all fields within a single subdomain are illustrated in Fig. 1.

While the components of the magnetic, electric, and bound charge polarization fields in a subdomain all require $(N_x + 1) \times (N_y + 1) \times (N_z + 1)$ values to be stored, the free
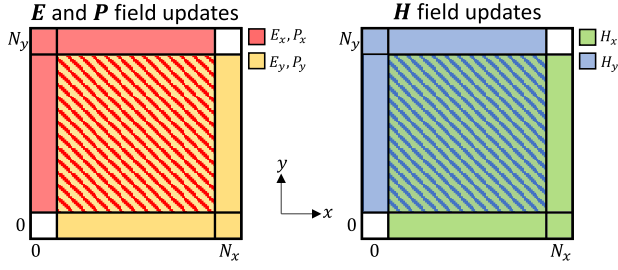
Fig. 1.   2-D representation of the field update regions within a subdomain for the electric/polarization fields (left) and the magnetic fields (right). Different colors are chosen to represent the different field components. The hatched regions indicate where both field components are updated.
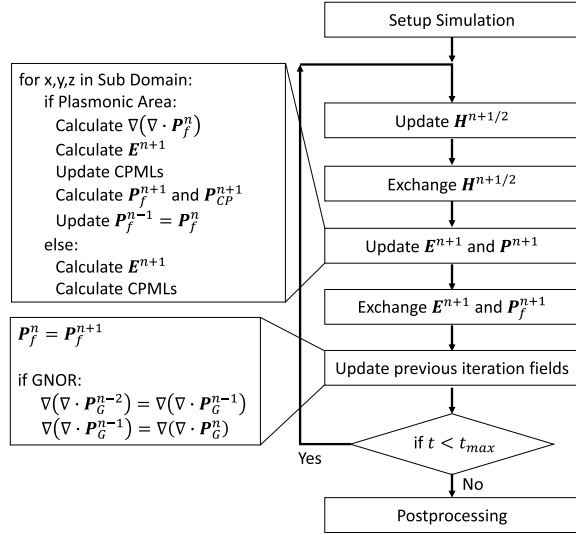

Fig. 2.   FDTD algorithm for the nonlocal Drude and GNOR models in an MPI framework.
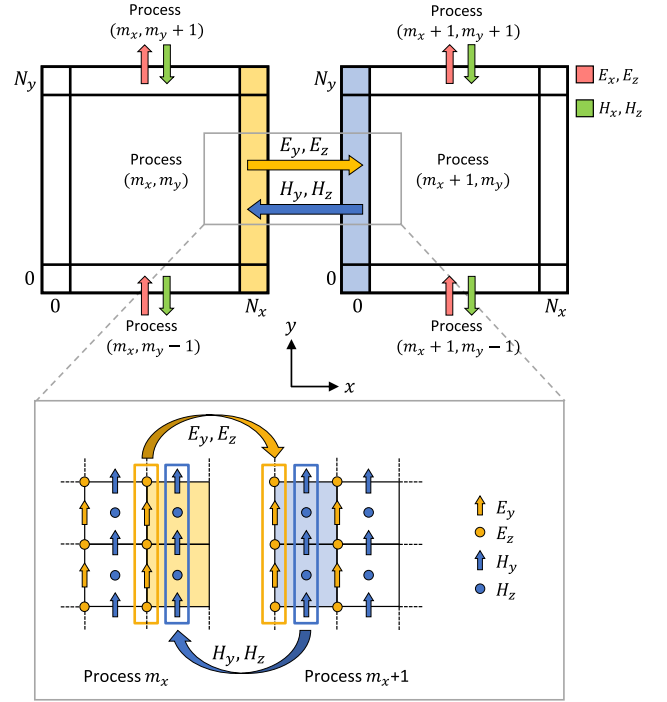

Fig. 3.   2-D representation of magnetic and electric field data transfers between adjacent subdomains. The different colors represent the different field components as indicated. The inset illustrates all field component transfers along x, and their relative positions in the Yee cell.

charge polarization fields requires $(N_x + 2) \times (N_y + 2) \times (N_z + 2)$. This is because the free charge polarization field updates via (18) requires information from additional cells. For example, to update $P_{x,NL}(0, j, k)$ via (18a), we need $P_{x,NL}(-1, j, k)$; in general, we need an extra cell in each dimension to store the -1 index. However, we do not calculate updates at this index, as $(-1, j, k)$ in subdomain (m_x, m_y, m_z) obtain their values from a transfer of data from cells $(N_x - 1, j, k)$ in subdomain $(m_x - 1, m_y, m_z)$.

We now discuss the flow of the FDTD algorithm for both the nonlocal Drude and GNOR models, including what data needs to be communicated, and when. This is summarized in Fig. 2, and we go through each step in detail in the following.

The first update to execute after the setup of the simulation is that of the magnetic field via f_1. Once this has been completed in each subdomain, a subset of the magnetic field values at the subdomain boundaries must be communicated to adjacent subdomains. The necessary communications for H_x are given in the first row of Table III; those for the other components of **H** can be obtained from this table by an ordered permutation of $x \rightarrow y \rightarrow z$. The intersubdomain communications in the x and y directions are illustrated in the top part of Fig. 3. Note that the data transfers of the magnetic

fields are all made in the "backward" direction. The inset in Fig. 3 details all data transfers along x and their relative Yee cell positions. For example, $H_y(0, j, k)$ updated locally in subdomain $(m_x + 1, m_y, m_z)$ is passed to $H_y(N_x, j, k)$ in subdomain (m_x, m_y, m_z).

After the magnetic field data transfer, the electric field is updated in each subdomain via f_2, after which the bound and free charge polarization fields are updated in each subdomain via f_3 and f_4, respectively. Subsequently, a subset of their values at the subdomain boundaries needs to be communicated to adjacent subdomains. The necessary communications for E_x are given in the second row of Table III; again, those for the other components are obtained by an ordered permutation of $x \rightarrow y \rightarrow z$. The intersubdomain communications for the electric field in the x and y directions are also illustrated in the top part of Fig. 3, with further detail given in the inset. Unlike the magnetic field data transfers, those for the electric field are made in the "forward" direction. For example, $E_y(N_x, j, k)$ updated in subdomain (m_x, m_y, m_z), is passed to $E_y(0, j, k)$ in subdomain $(m_x + 1, m_y, m_z)$. Note that only the **E** and **H** components tangential to the direction of the data transfer need to be exchanged.

In general, FDTD updates for LRA polarization models only require the collocated electric and polarization field values so that the polarization field values need not be communicated to other subdomains. Thus, no communication is necessary for the bound charge polarization field $\mathbf{P}_{CP}$. This is not true for the nonlocal models. The necessary communications for the x component of $\mathbf{P}_f$ are given in the third row of Table III and visualized in the top part Fig. 4. The communication for the y
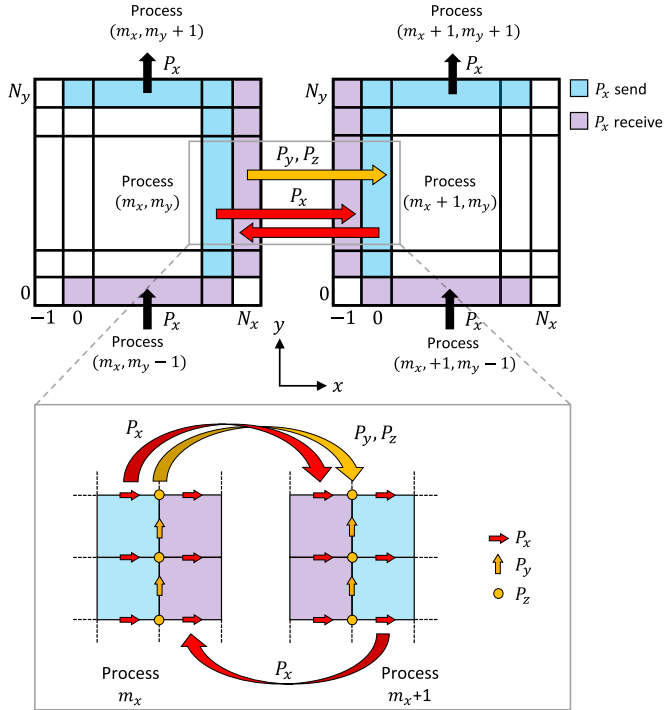
Fig. 4.   2-D representation of the data transfers between adjacent subdomains for the x component of the free charge polarization field. The $j = -1$ row in the y-direction is not shown or required for P_x, but would be required for P_y. The blue shade represents regions where P_x is locally calculated and sent to adjacent processes, and the purple represents regions where P_x is received from adjacent processes. The inset illustrates all free charge polarization field component transfers along x, and their relative positions in the Yee cell.

| H_x | Transfer $y = 0$ plane backward to adjacent $y = N_y$ plane |
	Transfer $z = 0$ plane backward to adjacent $z = N_z$ plane
E_x	Transfer $y = N_y$ plane forward to adjacent $y = 0$ plane
	Transfer $z = N_z$ plane forward to adjacent $z = 0$ plane
$P_{f,x}$	Transfer $x = 0$ plane backward to adjacent $x = N_x$ plane
	Transfer $x = N_x - 1$ plane forward to adjacent $x = -1$ plane
	Transfer $y = N_y$ plane forward to adjacent $y = 0$ plane
	Transfer $z = N_z$ plane forward to adjacent $z = 0$ plane
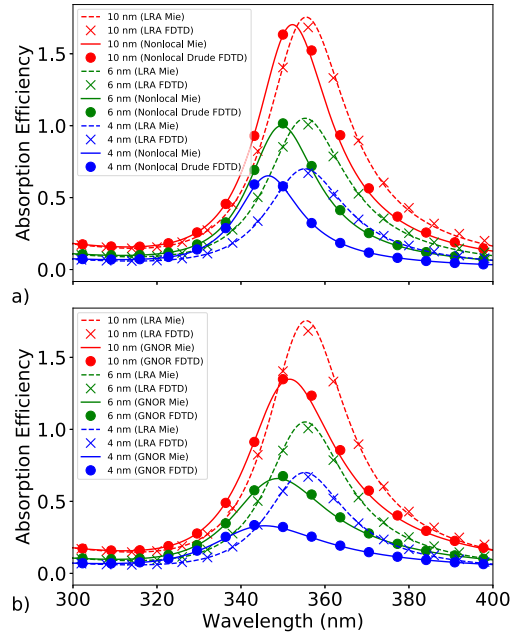
Fig. 5.   Absorption cross sections for silver spheres of diameter 4 nm (blue), 6 nm (green), and 10 nm (red) using (a) nonlocal Drude FDTD (filled circles) and (b) GNOR FDTD (filled circles). The solid lines represent the nonlocal Mie theory solutions (a) without diffusion and (b) with diffusion. The dashed lines in both plots represent the LRA Mie theory solutions and the x's represent the LRA FDTD solutions.

and z field components are obtained from Table III again via an ordered permutation of $x \rightarrow y \rightarrow z$. The inset of Fig. 4 shows the data transfers along x for all field components. Note that there are now four data transfers for every $\mathbf{P}_f$ component—three "forward" and one "backward"—due to the increased data required for updates via (18). Thus, the inclusion of nonlocality doubles the number of communications required at each time-step. This has an effect on performance and scalability and is discussed further in Section V.

It is worth noting that MPI is not the only solution for parallel computing as new higher-level languages are being introduced for this purpose. Chapel, a language produced by Cray [32], allows for algorithm implementation on a distributed system without the challenges of MPI. For example, [40] presents a finite difference implementation of Poisson's equation in Chapel. One may also use a shared memory implementation where the memory is shared amongst the processes (or threads) and therefore no data need be communicated. This can be implemented via OpenMP [41] for multithreading on CPUs or via CUDA [42] or OpenCL [43] on graphics processing units (GPUs). Indeed, GPU-FDTD implementations are well reported in literature [44]. Since GPUs can launch thousands of parallel threads that all have access to shared memory, a GPU-based implementation of nonlocal FDTD requires no special treatment beyond what was presented in Section III. While GPUs do suffer from memory constraints, they can still be useful for smaller nonlocal plasmonic simulations.

V. NONLOCAL FDTD APPLIED TO SMALL SPHERES

In this section, we test and validate our FDTD implementations of the nonlocal models by using them to simulate the optical response of small silver nanospheres. We compare our results to: 1) analytic solutions based on Mie theory, 2) LRA FDTD plasmonic simulations that employ the LRA Drude model for free-electron response, and 3) experimental results from the literature. Not only do our nonlocal FDTD simulations agree well with analytic and experimental results, but we also find an unexpected benefit over the LRA approach: a pronounced reduction of staircasing artifacts.

In Fig. 5, we plot the absorption efficiencies for silver nanospheres in vacuum for three different diameters—4 nm (blue), 6 nm (green) and 10 nm (red)—and different free charge polarization models. To model silver, we use the fitting parameters reported in [45] for ω_p and γ in (8) and (9), and for all critical points model parameters in (10). We set $\beta^2 = 1/3 v_F^2$ where $v_F = 1.39 \cdot 10^6$ m/s [46].

The FDTD domain is a 200 cell $\times$ 200 cell $\times$ 200 cell box truncated by a convolutional perfectly matched

layer (CPML) [38] consisting of 20 additional cells at each boundary. We use a uniform step-size of $\Delta x = \Delta y = \Delta z = 0.04, 0.06,$ and 0.1 nm for the 4, 6, and 10 nm particles, respectively, which equates to $D/100$, where D is the diameter of the sphere. For the particle sizes of interest here, this guarantees both that the step-size is less than the Fermi wavelength, and that the spherical shape is sufficiently resolved. Convergence tests confirmed that these step-sizes were sufficient. The total number of iterations varies with step-size and therefore particle size. For a 10 nm diameter particle, $3 \cdot 10^5$ iterations are used to reach convergence; this is scaled appropriately for the other particle sizes.

In Fig. 5(a), we compare our nonlocal Drude FDTD calculations (filled circles) with LRA FDTD calculations (x's), classical (LRA) Mie theory solutions (dashed lines), and with nonlocal Mie theory solutions (solid lines). Nonlocal Mie theory [47]–[49] is a modified version of Mie theory [50] that allows for longitudinal modes, which permits a nonzero free charge density within the nanoparticle. It has been successfully validated with experimental results for small particles larger than several nanometers. For example, a quasistatic version predicted absorption peaks that agree quantitatively with experiment for particle diameters down to 10 nm with a further qualitative agreement down to 2 nm [19].

We find in Fig. 5(a) excellent agreement between nonlocal Drude FDTD and nonlocal Mie theory, with less than 2% mean error for all three particle sizes. Doubling the FDTD step-size increases the mean error for the 10 nm particle case to 6.4%. Halving the step-size decreases it to 1.3%. Thus, reasonable convergence is reached with reasonable simulation domain sizes. As expected, we see an increasing blue-shift in the absorption peak with decreasing nanoparticle size with respect to the LRA model.

In Fig. 5(b) we compare our GNOR-FDTD calculations (filled circles) with LRA FDTD calculations (x's), LRA Mie theory solutions (dashed lines), and nonlocal diffusive Mie theory solutions (solid lines), where diffusion is accounted for by substituting β^2 with $\beta^2 + \mathcal{D}\gamma - i\mathcal{D}\omega$ in nonlocal Mie theory [17]. The free electron diffusion coefficient in silver is taken as $\mathcal{D} = 3.61 \times 10^{-4}$ m^2/s [17]. We again see excellent agreement, with less than 1.6% mean error in GNOR-FDTD relative to nonlocal diffusive Mie theory for all three particle sizes. As expected the resonance positions predicted by the nonlocal Drude FDTD in Fig. 5(a) and GNOR FDTD in Fig. 5(b) are the same, with an increased linewidth for GNOR FDTD.

For the simulations of Fig. 5, we also tracked the CPU time. For the 4 nm sphere simulations (256 cores) we report 155, 166, and 135 thousand time steps per hour for the LRA, nonlocal Drude, and GNOR FDTD simulations, respectively. Similarly, we report 278, 102, and 91 thousand time steps per hour for the 6 nm sphere (128 cores) and 200, 63, and 47 thousand time steps per hour for the 10 nm sphere (64 cores). Note that the supercomputer used for these simulations was comprised of cores that were not all the same speed, which may explain why the time step rate of the 4 nm LRA FDTD simulation is proportionally lower than it should be. In general, the LRA model is faster than the
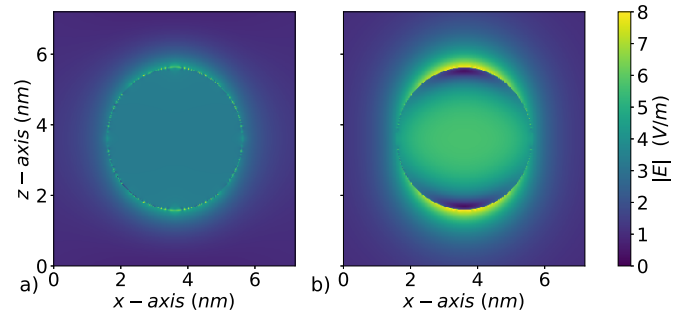

Fig. 6. Electric field amplitude distribution of a 4 nm diameter silver sphere in vacuum at $\lambda = 343$ nm using (a) LRA FDTD and (b) nonlocal Drude FDTD.
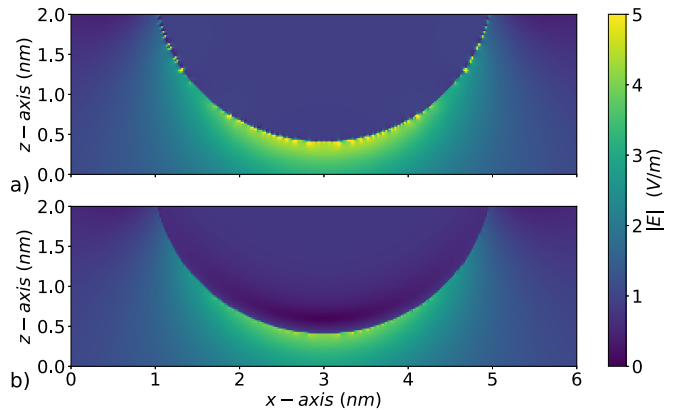

Fig. 7. Close-up of the electric field amplitude distribution of a 4 nm diameter silver sphere in vacuum at $\lambda = 425$ nm. Staircasing artifacts are much more prominent in (a) for LRA FDTD than in (b) for nonlocal Drude FDTD.

nonlocal models and GNOR is slower than the nonlocal Drude model.

We now turn to examine the near-field and free electron density distributions produced by nonlocal Drude FDTD, comparing to those produced by LRA FDTD. In Fig. 6 we show the electric field amplitude distribution for the simulations of the 4 nm diameter silver nanoparticle produced by (a) LRA FDTD and (b) nonlocal Drude FDTD, for the wavelength corresponding to the peak of the (nonlocal) absorption spectrum ($\lambda = 343$ nm). Shown are cuts in the xz-plane through the center of the particle, where the incident plane wave is z-polarized and propagates along the y-axis. The field amplitudes are normalized, corresponding to an input field of 1 V/m. For higher quality images, we used a halved step size of $\Delta x = D/200$. LRA FDTD produces a constant electric field within the sphere, as expected, while nonlocal Drude FDTD produces a field gradient due to the nonzero free charge distribution.

We see in Fig. 6 a significant difference in the appearance of the fields at the particle boundary. While the effects of staircasing in LRA FDTD are clearly visible at the edges of the sphere in Fig. 6(a), they appear smoothed out for nonlocal Drude FDTD in Fig. 6(b). This is even more evident in Fig. 7 which shows the normalized electric field amplitude distribution produced by (a) LRA FDTD and (b) nonlocal
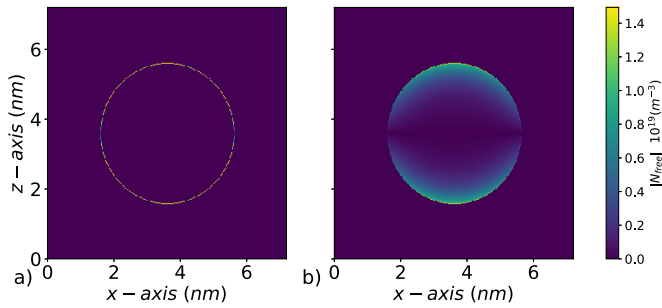
Fig. 8.   Free electron density within a 4 nm diameter silver sphere in vacuum at $\lambda = 343$ nm using (a) LRA FDTD and (b) nonlocal Drude FDTD.

Drude FDTD at $\lambda = 425$ nm, a wavelength where the absorption efficiency and near fields for both approaches are almost identical, except for dramatic differences at the sphere boundary. The staircasing-induced boundary artifacts seen for LRA FDTD are clearly reduced with nonlocal Drude FDTD. Interestingly, a smoothing effect in the presence of rough boundaries has been observed in nonlocal plasmonic FEM calculations [51]. In our case, however, the "roughness" is not due to a true physical boundary, but rather one that is artificially imposed on the structure due to the rectangular grid.

Artifacts at the particle boundary are especially problematic for calculations that involve fields just outside the particle, such as, for example, determining the plasmonic near field enhancement of fluorescence, or engineering the spontaneous emission lifetime of fluorophosphores [52]. This could also be important for calculations of plasmonics-enhanced nonlinear optics, where enhanced near fields close to plasmonic boundaries can be harnessed to not only enhance nonlinear optical processes by orders of magnitude, but also shape nonlinear optical fields [53]–[55]. With nonlocal FDTD, the reduction of staircasing artifacts would result in more reliable calculations.

In Fig. 8, we plot the free electron density distribution corresponding to the 4 nm silver particle simulations of Fig. 6. Shown are cuts in the xz plane through the center of the sphere for $\lambda = 343$ nm, as produced by (a) LRA FDTD and (b) nonlocal Drude FDTD. As expected, nonlocal Drude FDTD allows for the spread of the charge distribution near the particle boundary, which we see is on the order of the Fermi wavelength for silver, $\lambda_F = 0.5$ nm. In contrast, for LRA FDTD the charge is bound to the surface.

We present in the Supplementary Information (SI) time-domain movies for the 4 nm silver sphere simulations corresponding to Figs. 6–8 where the incident plane wave pulse function is a normalized raised cosine $f(t) = [(1 - \cos(\omega_{max}t))/2]^3$, where $\omega_{max} = 1.26 \cdot 10^{16}$ rad/s is the maximum frequency of interest (corresponding to $\lambda = 150$ nm). Included in the SI are movies of the electric field amplitude dynamics for nonlocal Drude FDTD in the xz and yz planes, *movie1*, and *movie2*, respectively, where both planes cut through the center of the particle. The comparable movies for LRA FDTD are *movie3* and *movie4*. The nonlocal FDTD movies show a radially propagating wave inside the sphere

whereas the LRA FDTD movies do not; in the latter, the field is almost always constant across the sphere (as expected). Furthermore, while staircasing artifacts in the LRA FDTD movies are quite pronounced, they are hardly visible in the nonlocal Drude FDTD movies. The corresponding free electron density movie for nonlocal Drude FDTD is *movie5*. Since the free electron density does not need to be tracked within the LRA FDTD implementation, and all charge is strictly localized to the surface, we do not include a time-domain movie for this case.

We now turn to further validate our FDTD implementations by comparing our simulated results to those of the experiment. In Ref. [13], electron energy loss spectroscopy measurements are presented for silver nanosphere diameters ranging from 2 to 24 nm on a carbon film (3 nm) and compared to Mie theory calculations that use size-dependent permittivities derived quantum mechanically. Using GNOR FDTD, we calculate the absorption spectra of silver nanospheres in a $n = 1.3$ dielectric background (as used in the calculations of Ref. [13]) with diameters ranging from 2 to 24 nm, and plot these in Fig. 9(a). Using the versatility inherent in FDTD, it is quite straightforward to include the effects of the carbon film, unlike what was done with Mie theory. We plot in Fig. 9(b) the absorption spectra of silver nanospheres on a 3 nm film of carbon ($n = 2$ according to Ref. [13]), where agreement with the experimental results was obtained only when a thin dielectric shell (radius of silver sphere/10, $n = 1.5$) around the silver particles was included, which could indicate that an oxide layer had formed. Thus, such FDTD simulations can be useful in helping determine the actual composition of the materials under experimental investigation.

We find the same trend as presented in Ref. [13], showing that GNOR FDTD is consistent with experimental measurements and calculations using quantum-based permittivities, with quantitative agreement down to 10 nm diameter, and qualitative agreement to 2 nm. As discussed in [17], for diameters less than 10 nm, the nonlocal model predicts a resonance shift that is not as large as determined by experimental measurements, which is consistent with our results. This may be due to more complicated phenomena occurring in silver, such as inhomogeneous equilibrium electron density, or spill-out effects, that are not included in the GNOR model we have implemented.

Finally, we turn to a discussion of computational resources and scalability. To give an example, for the 10, 6, and 4 nm sphere simulations presented in Fig. 5, we used 64, 128, and 256 cores, respectively, on the Graham cluster operated by Compute Canada [56]. Recall that the workload is heavier for the smallest particle since our step size Δx (and thus time step size) is proportional to sphere diameter, and thus more iterations in time are required to reach convergence for the smallest particles.

In general, when running simulations on a large number of cores, as we do for this article, it is imperative to investigate the implementation's scalability, that is, the performance enhancement obtained by increasing the number of CPUs. In the ideal case, the scaling is linear, meaning when one doubles the number of processes, the computation time is
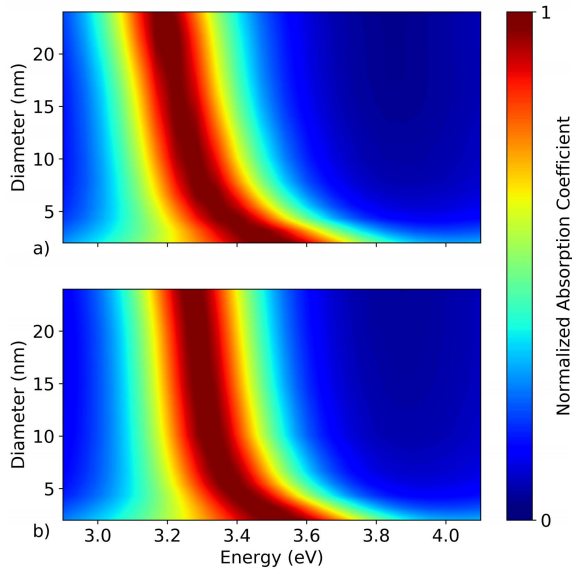
Fig. 9.   Contour plot of the absorption cross section of silver spheres (a) embedded in an $n = 1.3$ homogeneous dielectric background and (b) on a 3 nm carbon film with a thin $n = 1.5$ dielectric shell, as a function of incident plane wave photon energy (horizontal axis) and sphere diameter (vertical axis).
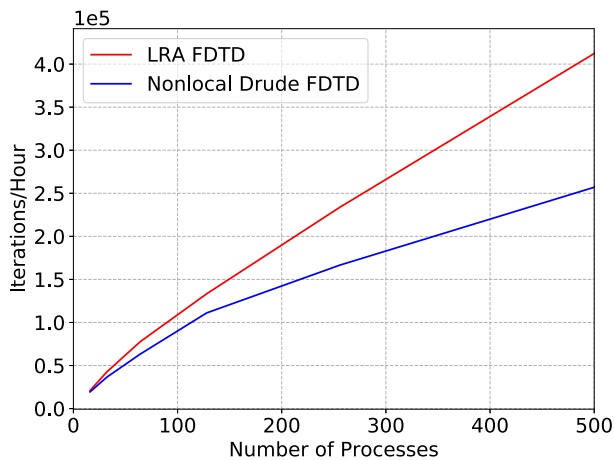

Fig. 10.   Scalability of the nonlocal Drude FDTD (blue line) compared to that of LRA FDTD (red line). Plotted is the number of FDTD time iterations computed per hour versus the number of processes used.

halved; this is often not achieved due to overhead, including interprocessor communications.

In Fig. 10, we plot the number of FDTD time iterations calculated per hour as a function of the number of processes used in the nonlocal Drude FDTD (blue line) and LRA FDTD (red line) simulations. The simulation set up is the same as for Fig. 5, where we vary the number of processes while keeping the total number of cells constant. For ≤ 128 processes, the scalability of nonlocal Drude FDTD is nearly linear and comparable to LRA FDTD. While the scalability of LRA FDTD remains mostly linear for a larger number of processes, that of nonlocal Drude FDTD does not, likely due to the doubled interprocess communication required, as discussed in Section IV. As one increases the number of processes while maintaining the same domain size, the subdomain surface-to-volume ratio increases, and therefore the inter-process communication time eventually becomes comparable
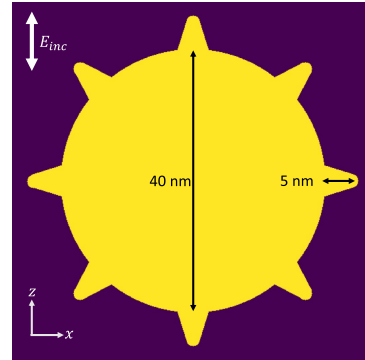

Fig. 11.   Cross section in the xz plane of the star-shaped silver nanoparticle, consisting of a sphere with 40 nm diameter and triangular nanoprism extrusions extending 5 nm from the sphere surface. The incident plane wave used to illuminate this structure is z-polarized and propagates along the y axis.

to the computation time within a time step. Thus, if we were to consider a larger domain size, we expect the near-linear scalability to extend to larger process numbers.

VI. Nonlocal FDTD Applied to Larger, Complex Nanoparticles

In this section, we demonstrate the benefit of our parallel FDTD implementation even further, by considering a much larger plasmonic structure containing small, sharp features. Such a structure would still be expected to exhibit nonlocal effects, and thus simulating it via FDTD would still require a small grid cell size, small enough to resolve electron dynamics within the sharp features. We consider as an example a structure inspired by the star-shaped nanoparticles synthesized for Ref. [57], which are spherical particles around 50 nm in diameter with small 5 nm extrusions from their surfaces that come to a sharp tip.

The structure we simulate is a silver nanosphere with triangular nanoprisms extruding from the equator in the xz plane, perpendicular to the incident plane wave propagation axis, as illustrated in Fig. 11. The sphere is 40 nm in diameter and the nanoprisms are embedded into the sphere so that the effective prism length is 5 nm. The tips of the nanoprisms are rounded with a radius of 1 nm. The FDTD step-size is uniform with $\Delta x = 0.1$ nm and the domain size is $600 \times 600 \times 600$ Yee cells (not including CPMLs). The simulations are run for $4 \cdot 10^5$ iterations over 1000 processes ($10 \times 10 \times 10$).

The absorption spectrum of this particle is shown in Fig. 12, calculated using both LRA FDTD (red) and nonlocal Drude FDTD (blue). There are two resonances attributed to the star-shaped particle. The peaks near 355 nm correspond to the plasmonic resonance of the sphere, and these completely overlap for the two models. This is expected, as nonlocal effects should be negligible for particles larger than 20 nm. The peaks near 575 nm, however, correspond to the resonance of the nanoprisms, specifically the ones aligned parallel to the incident field polarization. Here, we do see that nonlocal effects become important, as the peak wavelength predicted by nonlocal Drude FDTD is 10 nm blue-shifted from that predicted by LRA FDTD.
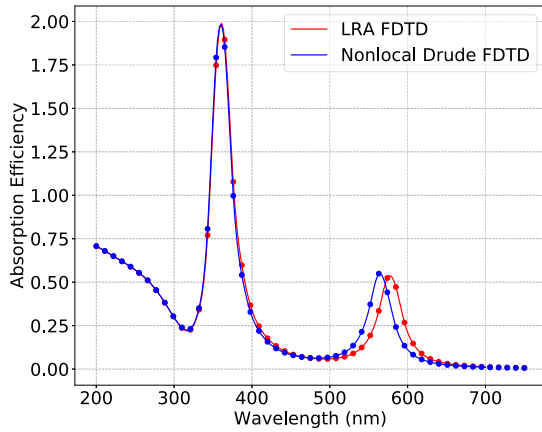
Fig. 12. Absorption efficiency of the silver star-shaped nanoparticle calculated using LRA FDTD (red dots) and nonlocal Drude FDTD (blue dots); the lines are interpolations of the FDTD data.
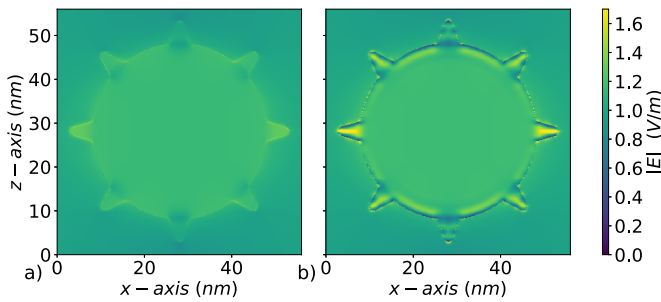

Fig. 13. Electric field amplitude distribution of a star-shaped nanoparticle in vacuum at $\lambda = 320$ nm using (a) LRA FDTD and (b) nonlocal Drude FDTD.

Additional differences between the two models manifest in the field amplitude distributions for wavelengths below the interband transition wavelength $\lambda_{IB} \approx 330$ nm. The electric field amplitude distributions at $\lambda = 320$ nm are shown in Fig. 13 for (a) LRA FDTD and (b) nonlocal Drude FDTD. Standing waves inside the vertical triangles, with a wavevector in the z-direction, are visible in Fig. 13(b) for nonlocal Drude FDTD. This is a longitudinal mode [18] and is expected since its wavelength lies below the epsilon-near-zero wavelength, which in silver is approximately equal to λ_{IB}. In the LRA, these modes cannot be excited by an incident transverse wave, and we see in Fig. 13(a) that they are not. However, with nonlocality, such excitation can occur [18] due to the additional material boundary conditions, discussed in Section III.

These standing waves become more pronounced for isolated nanotriangles as shown in Fig. 14(b) where nonlocal Drude FDTD was used, whereas they are absent in Fig. 14(a), where LRA FDTD was used. The standing waves found for nonlocal FDTD are damped by interband transitions for wavelengths below 300 nm.

We now turn to examine the effect of staircasing for the star-shaped nanoparticle. We show in Fig. 15 a zoomed-in view of the electric field amplitude distribution at $\lambda = 475$ nm, a wavelength where there is more contrast at the particle boundary than for the wavelength considered in Fig. 13. Despite a very fine mesh of $\Delta x = 0.1$ nm, one can clearly see staircasing artifacts in the electric field amplitude distribution
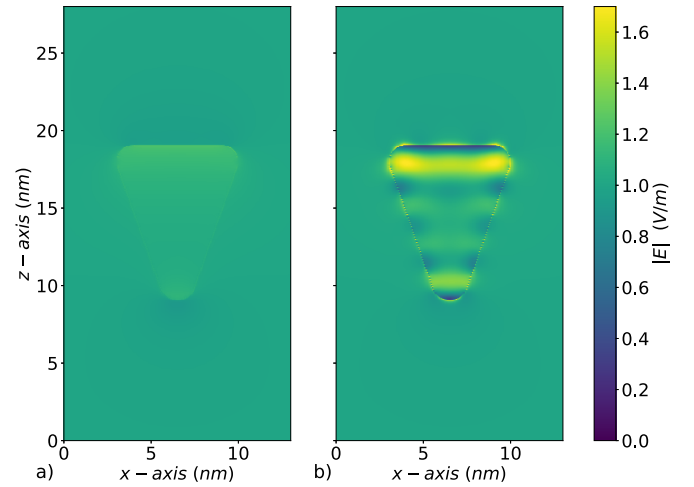

Fig. 14. Electric field amplitude distribution of isolated nanotriangles in vacuum at $\lambda = 320$ nm using (a) LRA FDTD and (b) the nonlocal Drude FDTD.
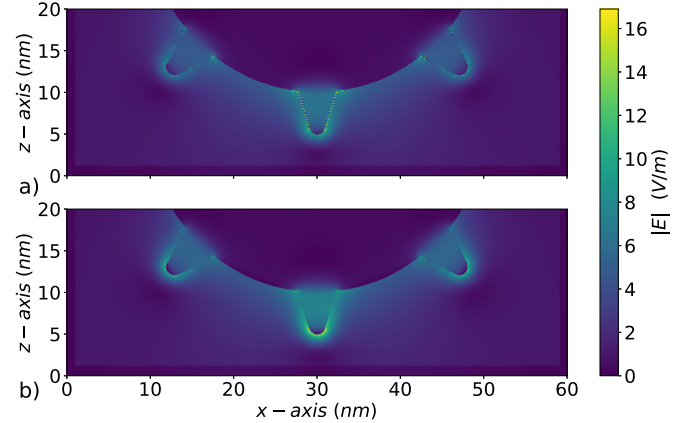

Fig. 15. Close up of the electric field distribution of the star-shaped particle at $\lambda = 475$ nm. The staircasing artifacts are much more prominent in (a) for LRA FDTD than in (b) for nonlocal Drude FDTD.

for LRA FDTD in Fig. 13(a). These are notably reduced in Fig. 13(b), where nonlocal Drude FDTD was used.

This reduction in staircasing artifacts is further illustrated by the time-domain movies of the star-shaped nanoparticle simulations presented in the SI. These depict the time evolution of the electric field amplitude and free electron density in the xz- and yz-planes through the center of the particle, where the incident plane wave is polarized in z and propagates along y. The electric field evolution movies for nonlocal Drude FDTD are *movie6* and *movie7*, while those for the corresponding free electron density evolution are *movie8* and *movie9*. The electric field evolution movies for LRA FDTD are *movie10* and *movie11*.

VII. CONCLUSION

We have introduced a parallel FDTD implementation for modeling nonlocality in plasmonics. We used an ADE approach to model nonlocality with and without electron diffusion and described in detail how to use the MPI framework for parallel computation via domain decomposition. After validating our implementation via comparisons with

analytical and experimental results for small nanospheres, we demonstrated the robustness of our parallel implementation for larger particles with sharp nanoscale features. We find that the inclusion of nonlocality within FDTD significantly reduces staircasing artifacts that can plague standard plasmonic FDTD modeling based on the LRA. This suggests that beyond its importance for modeling nonlocality, nonlocal FDTD might be advantageous for calculations that require precise values for the fields at plasmonic boundaries. This includes, for example, determining plasmonic fluorescence enhancement, plasmonics-mediated fluorescent lifetime engineering, and plasmonics enhanced nonlinear optics.

Acknowledgment

References

[1] V.-C. Su, C. H. Chu, G. Sun, and D. P. Tsai, "Advances in optical metasurfaces: Fabrication and applications [Invited]," *Opt. Exp.*, vol. 26, no. 10, pp. 13148–13182, May 2018. [Online]. Available: https://www.osapublishing.org/oe/abstract.cfm?uri=oe-26-10-13148

[2] J. A. Schuller, E. S. Barnard, W. Cai, Y. C. Jun, J. S. White, and M. L. Brongersma, "Plasmonics for extreme light concentration and manipulation," *Nature Mater.*, vol. 9, no. 3, pp. 193–204, Mar. 2010. [Online]. Available: https://www.nature.com/articles/nmat2630

[3] J. R. Mejía-Salazar and O. N. Oliveira, "Plasmonic biosensing," *Chem. Rev.*, vol. 118, no. 20, pp. 10617–10625, Oct. 2018. [Online]. Available: https://doi.org/10.1021/acs.chemrev.8b00359

[4] S. I. Bozhevolnyi and N. A. Mortensen, "Plasmonics for emerging quantum technologies," *Nanophotonics*, vol. 6, no. 5, pp. 1185–1188, Jan. 2017. [Online]. Available: https://www.degruyter.com/view/j/nanoph.2017.6.issue-5/nanoph-2016-0179/nanoph-2016-0179.xml

[5] M. Kauranen and A. V. Zayats, "Nonlinear plasmonics," *Nature Photon.*, vol. 6, no. 11, pp. 737–748, Nov. 2012. [Online]. Available: http://www.nature.com/articles/nphoton.2012.244

[6] F. Enrichi, A. Quandt, and G. C. Righini, "Plasmonic enhanced solar cells: Summary of possible strategies and recent results," *Renew. Sustain. Energy Rev.*, vol. 82, pp. 2433–2439, Feb. 2018. [Online]. Available: http://www.sciencedirect.com/science/article/pii/S136403211731239X

[7] N.-Y. Kim et al., "Localized surface plasmon-enhanced green quantum dot light-emitting diodes using gold nanoparticles," *RSC Adv.*, vol. 5, no. 25, pp. 19624–19629, Feb. 2015. [Online]. Available: https://pubs.rsc.org/en/content/articlelanding/2015/ra/c4ra15585h

[8] M. Sharifi et al., "Plasmonic gold nanoparticles: Optical manipulation, imaging, drug delivery and therapy," *J. Controlled Release*, vols. 311–312, pp. 170–189, Oct. 2019. [Online]. Available: http://www.sciencedirect.com/science/article/pii/S0168365919305164

[9] S. A. Maier, *Plasmonics: Fundamentals Application*. New York, NY, USA: Springer, 2007.

[10] P. G. Etchegoin, E. C. Le Ru, and M. Meyer, "An analytic model for the optical properties of gold," *J. Chem. Phys.*, vol. 125, no. 16, Oct. 2006, Art. no. 164705. [Online]. Available: http://aip.scitation.org/doi/10.1063/1.2360270

[11] U. Kreibig and L. Genzel, "Optical absorption of small metallic particles," *Surf. Sci.*, vol. 156, pp. 678–700, Jun. 1985. [Online]. Available: http://www.sciencedirect.com/science/article/pii/0039602885902390

[12] S. Raza, W. Yan, N. Stenger, M. Wubs, and N. A. Mortensen, "Blueshift of the surface plasmon resonance in silver nanoparticles: Substrate effects," *Opt. Exp.*, vol. 21, no. 22, pp. 27344–27355, Nov. 2013. [Online]. Available: https://www.osapublishing.org/oe/abstract.cfm?uri=oe-21-22-27344

[13] J. A. Scholl, A. L. Koh, and J. A. Dionne, "Quantum plasmon resonances of individual metallic nanoparticles," *Nature*, vol. 483, no. 7390, pp. 421–427, Mar. 2012. [Online]. Available: http://www.nature.com/articles/nature10904

[14] H. Baida et al., "Quantitative determination of the size dependence of surface plasmon resonance damping in single AgSiO$_2$ nanoparticles," *Nano Lett.*, vol. 9, no. 10, pp. 3463–3469, Oct. 2009. [Online]. Available: https://pubs.acs.org/doi/10.1021/nl901672b

[15] W. Zhu et al., "Quantum mechanical effects in plasmonic structures with subnanometre gaps," *Nature Commun.*, vol. 7, no. 1, Sep. 2016, Art. no. 011495. [Online]. Available: http://www.nature.com/articles/ncomms11495

[16] C. Ciraci et al., "Probing the ultimate limits of plasmonic enhancement," *Science*, vol. 337, no. 6098, pp. 1072–1074, Aug. 2012. [Online]. Available: http://www.sciencemag.org/cgi/doi/10.1126/science.1224823

[17] S. Raza, S. I. Bozhevolnyi, M. Wubs, and N. A. Mortensen, "Nonlocal optical response in metallic nanostructures," *J. Phys., Condens. Matter*, vol. 27, no. 18, May 2015, Art. no. 183204. [Online]. Available: http://stacks.iop.org/0953-8984/27/i=18/a=183204?key=crossref.8c354f8034f59793e8ac363e22b99808

[18] S. Raza, G. Toscano, A.-P. Jauho, M. Wubs, and N. A. Mortensen, "Unusual resonances in nanoplasmonic structures due to nonlocal response," *Phys. Rev. B, Condens. Matter*, vol. 84, no. 12, Sep. 2011, Art. no. 121412. [Online]. Available: https://link.aps.org/doi/10.1103/PhysRevB.84.121412

[19] S. Raza et al., "Blueshift of the surface plasmon resonance in silver nanoparticles studied with EELS," *Nanophotonics*, vol. 2, no. 2, pp. 131–138, 2013. [Online]. Available: https://www.degruyter.com/view/j/nanoph.2013.2.issue-2/nanoph-2012-0032/nanoph-2012-0032.xml

[20] N. A. Mortensen, S. Raza, M. Wubs, T. Søndergaard, and S. I. Bozhevolnyi, "A generalized non-local optical response theory for plasmonic nanostructures," *Nature Commun.*, vol. 5, no. 1, p. 3809, Sep. 2014. [Online]. Available: http://www.nature.com/articles/ncomms4809

[21] K. R. Hiremath, L. Zschiedrich, and F. Schmidt, "Numerical solution of nonlocal hydrodynamic Drude model for arbitrary shaped nano-plasmonic structures using Nédélec finite elements," *J. Comput. Phys.*, vol. 231, no. 17, pp. 5890–5896, Jul. 2012. [Online]. Available: http://www.sciencedirect.com/science/article/pii/S0021999112002550

[22] N. Schmitt, J. Viquerat, C. Scheid, S. Lanteri, M. Moeferdt, and K. Busch, "A 3D discontinuous Galerkin time-domain method for nano plasmonics with a nonlocal dispersion model," in *Proc. Prog. Electromagn. Res. Symp.-Spring (PIERS)*, May 2017, pp. 2792–2799.

[23] X. Zheng, M. Kupresak, R. Mittra, and G. A. E. Vandenbosch, "A boundary integral equation scheme for simulating the nonlocal hydrodynamic response of metallic antennas at deep-nanometer scales," *IEEE Trans. Antennas Propag.*, vol. 66, no. 9, pp. 4759–4771, Sep. 2018. [Online]. Available: https://ieeexplore.ieee.org/document/8399847

[24] J. Niegemann, W. Pernice, and K. Busch, "Simulation of optical resonators using DGTD and FDTD," *J. Opt. A, Pure Appl. Opt.*, vol. 11, no. 11, Nov. 2009, Art. no. 114015. [Online]. Available: https://iopscience.iop.org/article/10.1088/1464-4258/11/11/114015

[25] A. F. Oskooi, D. Roundy, M. Ibanescu, P. Bermel, J. D. Joannopoulos, and S. G. Johnson, "MEEP: A flexible free-software package for electromagnetic simulations by the FDTD method," *Comput. Phys. Commun.*, vol. 181, no. 3, pp. 687–702, Mar. 2010. [Online]. Available: http://www.sciencedirect.com/science/article/pii/S001046550900383X

[26] A. C. Lesina, A. Vaccari, P. Berini, and L. Ramunno, "On the convergence and accuracy of the FDTD method for nanoplasmonics," *Opt. Exp.*, vol. 23, no. 8, pp. 10481–10497, Apr. 2015. [Online]. Available: https://www.osapublishing.org/oe/abstract.cfm?uri=oe-23-8-10481

[27] J. M. McMahon, *Topics in Theoretical and Computational Nanoscience: From Controlling Light at the Nanoscale to Calculating Quantum Effects With Classical Electrodynamics* (Springer Theses). New York, NY, USA: Springer-Verlag, 2011. [Online]. Available: https://www.springer.com/gp/book/9781441982483

[28] L. Zhang, "FDTD algorithm for plasmonic nanoparticles with spatial dispersion," M.S. thesis, Dept. Elect. Comput. Eng., Ohio State Univ., Columbus, OH, USA, 2016. [Online]. Available: https://etd.ohiolink.edu/pg_10?0::NO:10:P10_ACCESSION_NUM:osu1452174003

[29] S. Bhardwaj, F. L. Teixeira, and J. L. Volakis, "Fast modeling of terahertz plasma-wave devices using unconditionally stable FDTD methods," *IEEE J. Multiscale Multiphys. Comput. Techn.*, vol. 3, pp. 29–36, 2018. [Online]. Available: https://ieeexplore.ieee.org/document/8338149/

[30] B. Gallinet, J. Butet, and O. J. F. Martin, "Numerical methods for nanophotonics: Standard problems and future challenges," *Laser Photon. Rev.*, vol. 9, no. 6, pp. 577–603, Nov. 2015. [Online]. Available: http://doi.wiley.com/10.1002/lpor.201500122

[31] K. Yee, "Numerical solution of initial boundary value problems involving Maxwell's equations in isotropic media," *IEEE Trans. Antennas Propag.*, vol. AP-14, no. 3, pp. 302–307, May 1966.

[32] *Chapel: Productive Parallel Programming*. Accessed: Sep. 4, 2019. [Online]. Available: https://chapel-lang.org/

[33] W. H. P. Pernice, "Finite-difference time-domain methods and material models for the simulation of metallic and plasmonic structures," *J. Comput. Theor. Nanosci.*, vol. 7, no. 1, pp. 1–14, Jan. 2010. [Online]. Available: http://openurl.ingenta.com/content/xref?genre=article&issn=1546-1955&vo lume=7&issue=1&spage=1

[34] M. Fang, Z. Huang, W. E. I. Sha, and X. Wu, "Maxwell–hydrodynamic model for simulating nonlinear terahertz generation from plasmonic metasurfaces," *IEEE J. Multiscale Multiphys. Comput. Techn.*, vol. 2, pp. 194–201, 2017. [Online]. Available: http://ieeexplore.ieee.org/document/8031967/

[35] U. Kreibig and C. V. Fragstein, "The limitation of electron mean free path in small silver particles," *Zeitschrift für Physik*, vol. 224, no. 4, pp. 307–323, Aug. 1969. [Online]. Available: http://link.springer.com/10.1007/BF01393059

[36] I. Tokatly and O. Pankratov, "Hydrodynamic theory of an electron gas," *Phys. Rev. B, Condens. Matter*, vol. 60, no. 23, pp. 15550–15553, Dec. 1999. [Online]. Available: https://link.aps.org/doi/10.1103/PhysRevB.60.15550

[37] K. P. Prokopidis and D. C. Zografopoulos, "A unified FDTD/PML scheme based on critical points for accurate studies of plasmonic structures," *J. Lightw. Technol.*, vol. 31, no. 15, pp. 2467–2476, Aug. 2013.

[38] A. Taflove and S. C. Hagness, *Computational Electrodynamics: The Finite-Difference Time-Domain Method* (Artech House Antennas and Propagation Library), 3rd ed. Boston, MA, USA: Artech House, 2005.

[39] B. Fornberg, "Generation of finite difference formulas on arbitrarily spaced grids," *Math. Comput.*, vol. 51, no. 184, pp. 699–706, Jan. 1988. [Online]. Available: http://www.ams.org/jourcgi/jour-getitem?pii=S0025-5718-1988-0935077-0

[40] R. Barrett, P. Roth, and S. Poole, "Finite difference stencils implemented using chapel," Future Technol. Group, Comput. Sci. Math. Division, Oak Ridge Nat. Lab., Oak Ridge, TN, USA, Tech. Rep. TM-2007/119, 2007.

[41] OpenMP. *en-GB OpenMP*. Accessed: Sep. 4, 2019. [Online]. Available: https://www.openmp.org/

[42] NVIDIA Developer. (Mar. 2014). *CUDA*. [Online]. Available: https://developer.nvidia.com/about-cuda

[43] The Khronos Group. (Jul. 2013). *OpenCL*. [Online]. Available: https://www.khronos.org/opencl/

[44] V. Demir and A. Z. Elsherbeni, "Compute unified device architecture (CUDA) based finite-difference time-domain (FDTD) implementation," *ACES J.-Appl. Comput. Electromagn. Soc.*, vol. 25, no. 4, p. 303, 2010.

[45] A. Vial, T. Laroche, M. Dridi, and L. Le Cunff, "A new model of dispersion for metals leading to a more accurate modeling of plasmonic structures using the FDTD method," *Appl. Phys. A, Solids Surf.*, vol. 103, no. 3, pp. 849–853, Jun. 2011. [Online]. Available: http://link.springer.com/10.1007/s00339-010-6224-9

[46] C. Kittel, *Introduction to Solid State Physics*, 8th ed. Hoboken, NJ, USA: Wiley, 2005.

[47] R. Ruppin, "Optical properties of a plasma sphere," *Phys. Rev. Lett.*, vol. 31, no. 24, pp. 1434–1437, Dec. 1973. [Online]. Available: https://link.aps.org/doi/10.1103/PhysRevLett.31.1434

[48] R. Ruppin, "Optical properties of small metal spheres," *Phys. Rev. B, Condens. Matter*, vol. 11, no. 8, pp. 2871–2876, Apr. 1975. [Online]. Available: https://link.aps.org/doi/10.1103/PhysRevB.11.2871

[49] A. Pack, M. Hietschold, and R. Wannemacher, "Failure of local Mie theory: Optical spectra of colloidal aggregates," *Opt. Commun.*, vol. 194, nos. 4–6, pp. 277–287, Jul. 2001. [Online]. Available: http://www.sciencedirect.com/science/article/pii/S0030401801013104

[50] H. C. Van der Hulst, *Light Scattering by Small Particles*. New York, NY, USA: Dover, 1981.

[51] A. Wiener, A. I. Fernández-Domínguez, A. P. Horsfield, J. B. Pendry, and S. A. Maier, "Nonlocal effects in the nanofocusing performance of plasmonic tips," *Nano Lett.*, vol. 12, no. 6, pp. 3308–3314, Jun. 2012. [Online]. Available: https://pubs.acs.org/doi/10.1021/nl301478n

[52] D. V. Guzatov, S. V. Vaschenko, V. V. Stankevich, A. Y. Lunevich, Y. F. Glukhov, and S. V. Gaponenko, "Plasmonic enhancement of molecular fluorescence near silver nanoparticles: Theory, modeling, and experiment," *J. Phys. Chem. C*, vol. 116, no. 19, pp. 10723–10733, May 2012. [Online]. Available: http://pubs.acs.org/doi/10.1021/jp301598w

[53] G. Li, S. Zhang, and T. Zentgraf, "Nonlinear photonic metasurfaces," *Nature Reviews Materials*, vol. 2, no. 5, Mar. 2017, Art. no. 017010. [Online]. Available: https://www.nature.com/articles/natrevmats201710

[54] A. Krasnok, M. Tymchenko, and A. Alù, "Nonlinear metasurfaces: A paradigm shift in nonlinear optics," *Mater. Today*, vol. 21, no. 1, pp. 8–21, Jan./Feb. 2018. [Online]. Available: http://www.sciencedirect.com/science/article/pii/S136970211730233X

[55] S. Keren-Zur, L. Michaeli, H. Suchowski, and T. Ellenbogen, "Shaping light with nonlinear metasurfaces," *Adv. Opt. Photon.*, vol. 10, no. 1, pp. 309–353, Mar. 2018. [Online]. Available: https://www.osapublishing.org/aop/abstract.cfm?uri=aop-10-1-309

[56] *Graham—CC Doc*. Accessed: Sep. 4, 2019. [Online]. Available: https://docs.computecanada.ca/wiki/Graham

[57] L. Minati, F. Benetti, A. Chiappini, and G. Speranza, "One-step synthesis of star-shaped gold nanoparticles," *Colloids Surf. A, PhysicoChem. Eng. Aspects*, vol. 441, pp. 623–628, Jan. 2014. [Online]. Available: http://www.sciencedirect.com/science/article/pii/S0927775713007796
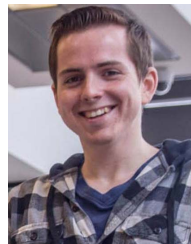
Joshua Baxter received the B.Sc. degree in physics/mathematics from the University of Ottawa, Ottawa, ON, Canada, in 2017 and started the M.Sc. degree in the same year. He transferred to the Ph.D. degree in 2019.

His work has involved plasmonic coloring with ultrafast lasers, simulations of laser heating, and computational nanophotonics. His current work focuses on deep learning applications to nanophotonics, nonlinear plasmonics via hydrodynamics, and active metasurfaces.

Mr. Baxter was awarded a Vanier Canada Graduate Scholarship from the Natural Sciences and Engineering Research Council in 2020.

Antonio Calà Lesina received the B.Sc. degree in electronics engineering in 2006 and the M.Sc. degree in telecommunications engineering in 2009 from the University of Catania, Catania, Italy, and the Ph.D. degree in information and communication technologies (computational electromagnetics) from the University of Trento, Trento, Italy, in 2013.

In 2009, he joined the Fondazione Bruno Kessler and the University of Trento. From 2013 to 2020, he worked at the University of Ottawa, Ottawa, ON, Canada, in the groups of Professors Lora Ramunno and Pierre Berini, where he conducted his research on computational nanophotonics, plasmonic coloring, photonics design, nonlinear metasurfaces and optical phased arrays. He is a Professor (W2, tenure-track) with Leibniz Universität Hannover, Hannover, Germany, since 2020.
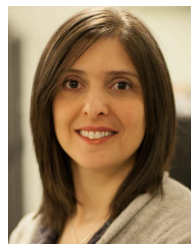
Lora Ramunno received the Ph.D. degree in physics from the University of Toronto, Toronto, ON, Canada, in 2002.

After a year in a high-tech startup, she returned to academia as a Post-Doctoral Fellow with University of Ottawa (UOttawa), Ottawa, ON. Since 2007, she has been a Faculty Member in Physics with UOttawa, where she is currently a Full Professor. Her theoretical/computational research focuses on nonlinear and nano-optics, including intense laser-matter interaction, nanophotonics, nonlinear optical microscopy, and photonic devices.

Dr. Ramunno held a Canada Research Chair in Computational Nanophotonics from 2007 to 2017 and was the recipient of an Early Researcher Award in 2007. She also has several successful industrial collaborative projects. She is a fellow of the Max-Planck-UOttawa Centre for Extreme and Quantum Photonics, a fellow of the NRC-UOttawa Joint Centre for Extreme Photonics, and a member of the UOttawa Centre for Research in Photonics.